ROYAL SOCIETY
OF CHEMISTRY

EDGE ARTICLE

Check for updates

All publication charges for this article have been paid for by the Royal Society of Chemistry

Dynamic structural engineering of ferrocene-functionalized Ag$_{20}$ nanoclusters for enhanced CO$_2$ electroreduction performance

Hong-Yan Zhu,[a] Xiao-Wei Wang,[a] Xin-Yu Chen,[a] Lan-Yan Li,[b] Yi-Xin Li,[c] Wei Dong Yu,[b] Jun Yan [ID][a] and Chao Liu [ID] *[ad]

The integration of organometallic motifs with metal nanoclusters offers a powerful strategy for constructing hybrid catalysts with precisely tunable active sites. Here, we report the synthesis of a 20-silver nanocluster, **Ag$_{20}$-Fc**, *via* cooperative coordination between thiacalix[4]arene (TC4A) and ferrocenylacetylene ligands. The cluster adopts a distinctive sandwich-like architecture, featuring two Ag$_5$@TC4A units flanking a ferrocenyl-stabilized Ag$_{10}$ core, and exhibits excellent structural tunability. Ligand engineering allows replacement of the ferrocenylacetylene units with methoxyphenylacetylene (**Ag$_{20}$-OPh**) or phenylacetylene (**Ag$_{20}$-Ph**), while preserving the core framework. Electrospray ionization mass spectrometry reveals dynamic structural reorganization in solution, where Ag$_5$@TC4A fragments are capable of capturing Ag–alkyne species and reassembling into sandwich-type clusters—a process substantiated by the structural features of Ag$_{24}$, Ag$_{12}$, and Cu$_2$Ag$_{11}$. **Ag$_{20}$-Fc** generates a locally electron-rich environment and conjugated ethynyl bridges that facilitate directional charge transfer, delivering outstanding electrocatalytic CO$_2$ reduction. It achieves over 98% faradaic efficiency for CO across a wide potential range (−1.0 to −1.8 V *vs.* RHE) and maintains operational stability for 24 h, significantly outperforming **Ag$_{20}$-OPh** and **Ag$_{20}$-Ph**. Density functional theory calculations uncover a dual enhancement mechanism in which orbital hybridization between ferrocenyl groups and silver atoms tunes the electronic structure at active sites, resulting in a 0.28 eV reduction in the energy barrier for *COOH intermediate formation compared to **Ag$_{20}$-Ph**.

Introduction

The electrochemical reduction of carbon dioxide (eCO$_2$RR) has emerged as a promising carbon-neutral strategy, garnering increasing attention for its dual potential to mitigate greenhouse gas emissions and rebalance the carbon cycle *via* renewable electricity.[1–3] This reaction enables the conversion of CO$_2$ into value-added fuels and chemicals under ambient conditions, offering significant potential for sustainable energy and chemical production.[4–9] Despite this promise, practical deployment of eCO$_2$RR remains hindered by several key challenges: the thermodynamic stability and chemical inertness of CO$_2$, competing hydrogen evolution reaction (HER), and the complexity of selectively controlling multi-electron, multi-proton transfer pathways.[10–15]

To address these limitations, extensive efforts have been dedicated to developing advanced electrocatalysts capable of achieving high faradaic efficiencies, industrially relevant current densities, and long-term operational durability.[16–21] Among these, nanocatalysts with atomically defined structures have demonstrated significant potential in tuning catalytic activity and selectivity.[22–29] However, the bottom-up synthesis of such catalysts with precise control over size, geometry, and elemental composition remains a formidable challenge, emphasizing the need for innovative synthetic strategies.[30–32] In this context, ligand-protected metal nanoclusters (NCs), typically <3 nm in diameter, have emerged as a unique class of atomically precise materials situated at the interface between molecular and nanoscale domains.[33–40] These well-defined "superatoms" offer distinct advantages for catalytic applications, including atomic-level structural resolution *via* single-crystal X-ray diffraction (SCXRD), tailorable surface environments through ligand engineering, and hybrid electronic states originating from strong metal–ligand orbital coupling.[41–47] These features make NCs an ideal platform for probing structure–activity relationships and for the rational design of next-generation electrocatalysts.

[a]College of Chemistry and Chemical Engineering, Central South University, Changsha 410083, Hunan, P. R. China. E-mail: chaoliu@csu.edu.cn

[b]School of Resources and Environment, Hunan University of Technology and Business, Changsh 410000, P. R. China

[c]Key Laboratory of Advanced Energy Materials Chemistry (Ministry of Education), Nankai University, Tianjin 300071, China

*[d]State Key Laboratory of Structural Chemistry, P. R. China*

A critical requirement for efficient eCO_2RR is rapid and effective charge transport across the catalyst–electrode interface.[48] However, the insulating nature of traditional ligands used to stabilize NCs often impedes electron transfer, thereby compromising catalytic efficiency. To address this limitation, redox-active ligands such as metallocenes—particularly ferrocene and its derivatives—have emerged as promising molecular components.[49] These organometallic units exhibit outstanding redox reversibility, fast electron-transfer kinetics, and well-defined electrochemical properties. When integrated into NCs, metallocenes not only facilitate electronic communication between active sites and electrodes but also offer a means to modulate the structural and electronic configuration of the catalyst.[50–53] Nevertheless, the incorporation of metallocene moieties into atomically precise NCs remains underexplored, primarily due to the synthetic complexity and structural heterogeneity of conventional nanoparticle surfaces, which hinder atomic-level mechanistic understanding.

Herein, we report the design of a hybrid nanocatalyst, **Ag$_{20}$-Fc**, constructed by anchoring twelve ferrocenylacetylene ligands onto a thiacalix[4]arene (TC4A)-stabilized silver nanocluster. This atomically defined framework allows systematic investigation of ligand effects at the molecular level. Targeted ligand engineering further affords two analogues, **Ag$_{20}$-OPh** and **Ag$_{20}$-Ph**, by replacing ferrocenyl units with methoxyphenylacetylene and phenylacetylene, respectively, while preserving the Ag$_{20}$ core. Solution-phase electrospray ionization mass spectrometry (ESI-MS) revealed dynamic self-assembly behavior of the Ag$_{20}$ motif, wherein two Ag$_5$@TC4A fragments capture Ag–alkyne species and reorganize into sandwich-like architectures *via* well-defined intermediates. This structural adaptability underscores the modularity of the cluster framework and its suitability for mechanistic studies. Electrochemical characterization revealed a pronounced dependence of catalytic performance on the nature of surface ligands. Among the series, **Ag$_{20}$-Fc** exhibited superior electrocatalytic activity for CO_2 reduction, achieving a CO faradaic efficiency (FE) exceeding 98% over a wide potential window (-1.0 to -1.8 V *vs.* RHE) and demonstrating operational stability for over 24 hours. In contrast, both **Ag$_{20}$-OPh** and **Ag$_{20}$-Ph** displayed lower CO selectivity, with maximum FEs of ~91%. Density functional theory (DFT) calculations elucidated an enhancement mechanism in **Ag$_{20}$-Fc**: strong orbital hybridization between the ferrocenyl ligands and the silver core effectively modulates the local electronic structure, thereby reducing the energy barrier for *OCHO intermediate formation by 0.28 eV compared to **Ag$_{20}$-Ph**. These findings highlight the critical role of redox-active organometallic ligands in tuning both geometric and electronic properties at the active sites. Overall, this study establishes a rational design strategy that leverages organometallic ligand engineering to precisely tailor the surface and electronic environment of atomically defined nanoclusters, providing a powerful platform for the development of efficient and tunable electrocatalysts for CO_2 reduction.

Results and discussion

Synthesis and structure of Ag$_{20}$-Fc nanocluster Ag$_{20}$-Fc was synthesized *via* a one-pot solvothermal method by dissolving ferrocenylacetylene (Fc-C≡CH), Ag$_2$O, and TC4A in a CH$_3$CN/CH$_2$Cl$_2$ mixed solvent (Scheme 1). The solution was heated at 60 °C for 72 hours, resulting in the direct precipitation of yellow crystalline **Ag$_{20}$-Fc** with a yield of 62%. SCXRD analysis revealed that **Ag$_{20}$-Fc** crystallizes in the monoclinic system with space group $C2/c$, containing one cluster per unit cell. The molecular formula $\{Ag_{20}(TC4A)_2(Fc-C≡C)_{12}\}$ indicates an architecture composed of 20 Ag atoms, two TC4A ligands, and twelve ferrocene-alkynyl groups. The cluster adopts a sandwich-like prismatic structure (Fig. 1A), featuring two $\{Ag_5@TC4A\}$ caps flanking a central Ag$_{10}$ core stabilized by ferrocene-alkynyl ligands. Each TC4A ligand coordinates in a μ_5-$\kappa(O)^3{:}\kappa(O)^3{:}\kappa(O)^3{:}\kappa(O)^3{:}\kappa(S)^1{:}\kappa(S)^1{:}\kappa(S)^1{:}\kappa(S)^1$ binding mode, encapsulating a Ag5 unit (Fig. 1B). Four Ag$^+$ form a distorted square at the lower rim of TC4A, while an additional Ag$^+$ resides at the ligand's upper rim, secured by four Ag–O bonds and weak Ag···Ag interactions (2.976(5)–3.047(7) Å). The Ag$_{10}$ core exhibits a layered sandwich configuration (Fig. 1C), comprising a central Ag$_4$ planar square intersected by two perpendicular Ag$_3$ linear units. The Ag···Ag distances within the Ag$_{10}$ core range from 2.783(3) to 2.808(4) Å, consistent with argentophilic interactions (Fig. 1D). Twelve alkyne ligands bridge the Ag$_{10}$ core and $\{Ag_5@TC4A\}$ subunits (Fig. 1E), consolidating the cluster's cross-shaped geometry with C_{2v} symmetry.

Ligand Engineering of Ag$_{20}$ nanoclusters subtle modulation of ligand environments in Ag NCs can have profound effects on their physicochemical and catalytic properties.[49,50] However, direct structure–property comparisons between NCs with identical metal cores but distinct surface ligands remain scarce. To probe the influence of ferrocene-based ligands on cluster performance, we synthesized three analogues—one **Ag$_{20}$-Ph** (Fig. 2A) and two **Ag$_{20}$-OPh** (Fig. 2B and C) —by substituting ferrocenylacetylene with phenylacetylene (Ph-C≡CH) and *para*-methoxyphenylacetylene (OPh-C≡CH), respectively. Both derivatives were obtained through careful solvent system optimization and found to be isostructural with **Ag$_{20}$-Fc**. Structural analysis confirmed that all three clusters preserve a nearly identical Ag$_{20}$ core, with the primary differences residing in the
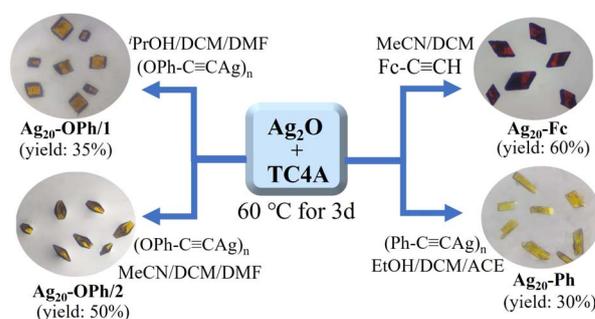
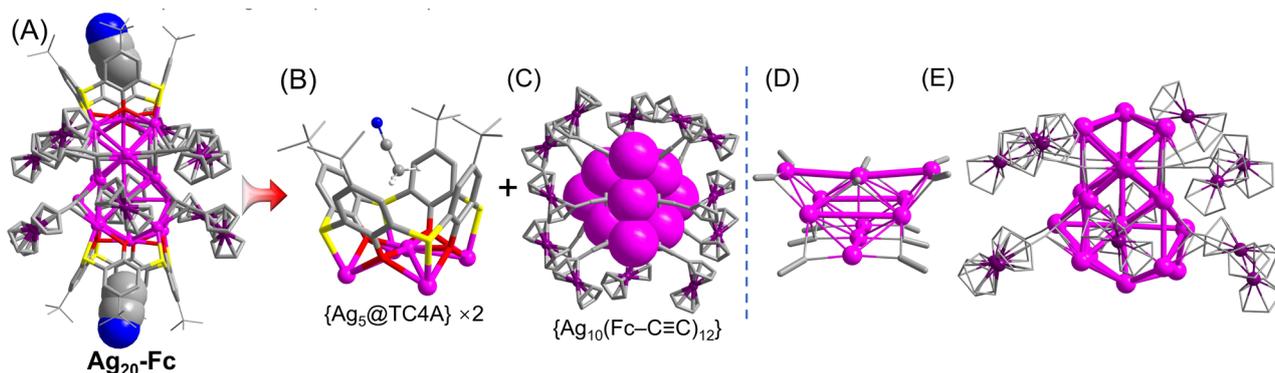**Scheme 1** Schematic illustration of the synthesis of the reported Ag$_{20}$ clusters.

Fig. 1 Crystal structure of the **Ag$_{20}$-Fc** cluster. (A) Overall molecular structure; (B) structure of the {Ag$_5$(TC4A)} secondary building unit (SBU); (C) Ag$_{10}$L$_{12}$ structural unit; (D) Ag$_{10}$ core; (E) Ag$_{20}$ metallic core.

electronic and steric nature of the terminal alkynyl ligands (Fig. 2D and E). Interestingly, variations were observed in the guest solvent molecules encapsulated within the TC4A cavities. In **Ag$_{20}$-Fc** and **Ag$_{20}$-OPh/2**, two CH$_3$CN molecules are hosted in the cavities, stabilized by C–H···π interactions with methyl groups oriented toward the cavity center. In contrast, **Ag$_{20}$-Ph** and **Ag$_{20}$-OPh/1** encapsulate CH$_2$Cl$_2$ and isopropanol, respectively. These guest-dependent differences induce varying degrees of distortion in the cluster frameworks. Notably, the two structural isomers of **Ag$_{20}$-OPh** exhibit significant conformational disparities in their Ag cores, attributed to the steric and electronic differences between CH$_3$CN and isopropanol within the TC4A host. These results highlight the sensitivity of cluster conformation to host–guest interactions.

Dynamic structural transformation and modular reorganization of the Ag$_{20}$ cluster in solution the Ag$_{20}$ cluster can be structurally described as a modular assembly composed of two {Ag$_5$(TC4A)} units bridged by a central Ag$_{10}$L$_{12}$ substructure. The Ag$_{10}$ core adopts a sandwich-like configuration, with a planar Ag$_4$ square flanked by two perpendicular linear Ag$_3$ units. Understanding the behavior of such a delicate architecture in solution is crucial for elucidating its self-assembly mechanism and evaluating its structural adaptability. To explore the

dynamic nature of Ag$_{20}$ in solution, three cluster variants—**Ag$_{20}$-Fc**, **Ag$_{20}$-OPh**, and **Ag$_{20}$-Ph**—were dissolved in CHCl$_3$ and analyzed by ESI-MS in positive-ion mode. Notably, no intact molecular ion was observed for **Ag$_{20}$-Fc**, likely due to the destabilizing steric effects of the bulky ferrocenyl ligands (Fig. 3A). In contrast, **Ag$_{20}$-OPh** exhibited a well-resolved peak at $m/z = 5467.08$, in excellent agreement with the calculated mass of {HAg$_{20}$(TC4A)$_2$(OPh-C≡C)$_{12}$(CHCl$_3$)$_2$(MeOH)$_2$}$^+$ ($m/z = 5467.00$). Meanwhile, **Ag$_{20}$-Ph** displayed a distinct peak at $m/z = 4805.95$, which closely matches the calculated mass of {HAg$_{20}$(TC4A)$_2$(Ph-C≡C)$_{12}$}$^+$ ($m/z = 4805.90$). These results suggest that smaller ligands enhance the solution-phase stability of the cluster.

Despite differences in overall stability, all three Ag$_{20}$ variants exhibited similar fragmentation behavior upon ESI-MS analysis. In the m/z 2000–3000 range, signals corresponding to {Ag$_9$(TC4A) ± (AgL)$_x$}$^+$ species were observed, while larger fragments such as {Ag$_{12}$(TC4A)$_2$ ± (AgL)$_x$}$^+$ appeared in the 3000–4000 range. These species, retaining one or two TC4A units, undergo systematic addition or loss of silver atoms and alkynyl ligands, indicative of a stepwise dissociation process. Combined with solid-state structural data, these observations reveal that Ag$_{20}$ is intrinsically dynamic in solution—capable of
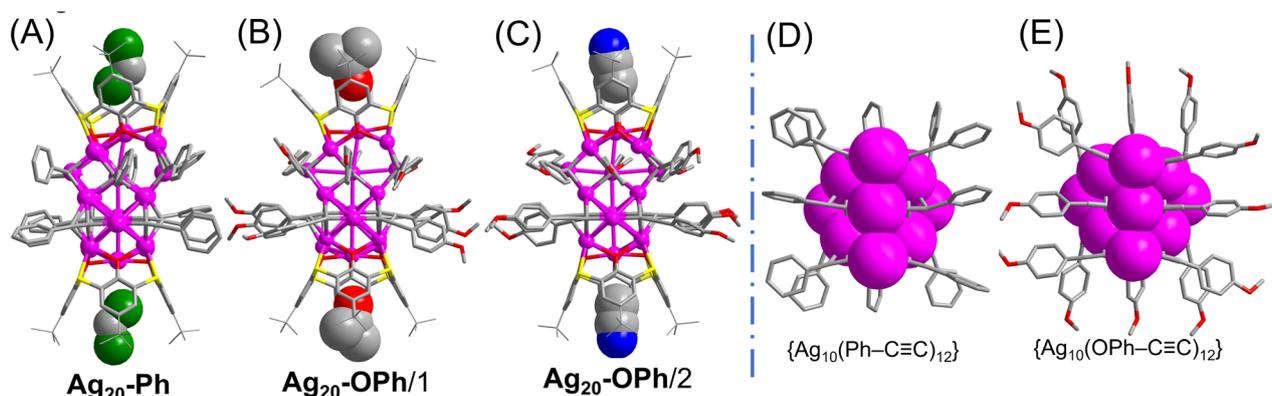

Fig. 2 Overall molecular structures of **Ag$_{20}$-Ph** (A), **Ag$_{20}$-OPh/1** (B), and **Ag$_{20}$-OPh/2** (C); Ag$_{10}$ core protected by phenylacetylene (D) and by *p*-methoxyphenylacetylene (E).
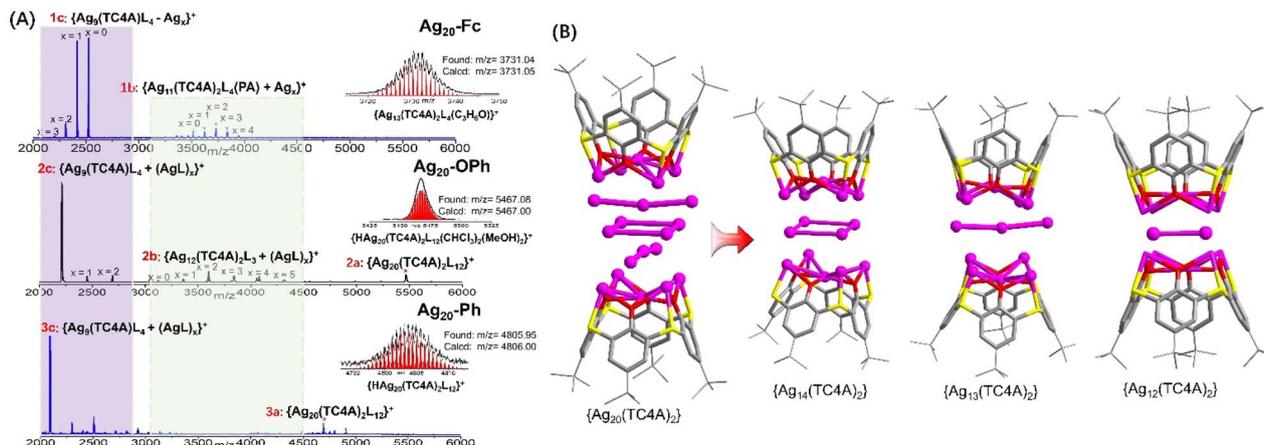
Fig. 3 (A) Positive-mode ESI-MS spectra of **Ag₂₀-Fc**, **Ag₂₀-OPh** and **Ag₂₀-Ph** in CH₂Cl₂ solution; (B) proposed structural disassembly pathway of the Ag_{20} cluster.

reversible dissociation into modular units such as $\{Ag_5(TC4A)\}$, followed by reassembly into higher-order architectures (Fig. 3B). This reversible, modular behavior underscores the hierarchical and adaptive character of Ag_{20} self-assembly in solution.

The dynamic reconfigurability of Ag_{20} is further supported by a series of structurally related clusters synthesized under comparable conditions. Clusters such as **Ag₁₂**, **Cu₂Ag₁₁**, and **Ag₂₄**—all assembled from TC4A and alkynyl ligands—can be rationalized as solution-phase transformation products of Ag_{20} through selective reorganization. For example, replacing ferrocenylacetylene with the less bulky *tert*-butylacetylene produces **Ag₁₂**, which retains the $\{Ag_5(TC4A)\}$ fragments while simplifying the core into an Ag_2L_4 dimer (Fig. 4A). **Cu₂Ag₁₁** preserves the overall sandwich-like motif of Ag_{20} but replaces the two $\{Ag_5(TC4A)\}$ caps with $\{CuAg_4(TC4A)\}$ units and reorganizes the $Ag_3–Ag_4–Ag_3$ core into a linear Ag_3 bridge (Fig. 4B). **Ag₂₄**, stabilized by trifluoromethylphenylacetylene ligands, displays an even more intricate structure, featuring a planar $Cl_2@Ag_9$ core surrounded by three $\{Ag_5@TC4A\}$ units arranged in trigonal symmetry (Fig. 4C). The $Cl_2@Ag_9$ motif consists of two Ag_5 pentagons sharing a common vertex, each embedding a Cl^- ion (Fig. 4D), with the anionic templates playing a pivotal role in directing geometric rearrangement and inducing symmetry

transformation relative to Ag_{20} (Fig. 4E). Together, these clusters—**Ag₁₂**, **Cu₂Ag₁₁**, and **Ag₂₄**—serve as structural snapshots of the Ag_{20} cluster's intrinsic dynamic and modular nature in solution. They demonstrate Ag_{20}'s capacity for reversible fragmentation and structural reorganization in response to variations in ligand identity, anionic templating, and solvent environment, highlighting its role not as a static species, but as a highly adaptive scaffold capable of tunable, hierarchical assembly.

Electrochemical CO_2 reduction Surface ligands are central to engineering the catalytic microenvironment and enhancing activity through multiple pathways.[54,55] Nonetheless, the multivariate synergistic interactions and generalizable design principles underlying ligand modulation remain elusive. Atomically precise metal clusters, with their well-defined structures and uniform active sites, represent ideal platforms for systematically dissecting these effects. In this study, the three Ag_{20} NCs with an identical metal core but distinct organic ligand shells were employed as a structurally controlled platform to investigate the influence of ligand engineering—specifically, organometallic functionalization—on the eCO₂RR. This model system provides unique insight into how surface chemistry affects the activity and selectivity of ultrasmall metal
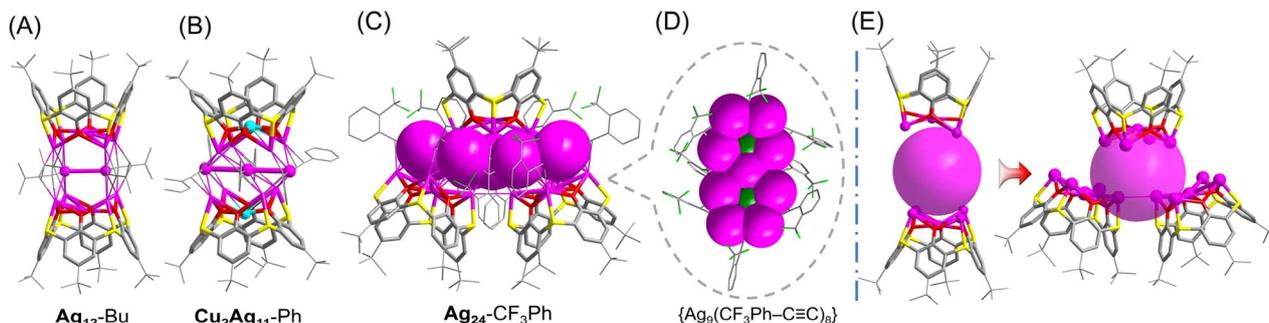

Fig. 4 Structures of the **Ag₁₂** (A), **Cu₂Ag₁₁** (B), and **Ag₂₄** (C) clusters; (D) $Cl_2@Ag_9L_8$ structural motif; (E) topological structural transformations from Ag_{20} to Ag_{24}.

catalysts. The CO_2RR performance of the clusters was initially assessed using a flow cell setup. Linear sweep voltammetry (LSV) measurements were conducted in CO_2- and N_2-saturated 1 M KOH solutions to evaluate the intrinsic catalytic activity. As shown in Fig. 5A, all three Ag_{20} NCs exhibited substantially higher current densities and more positive onset potentials under CO_2-saturated conditions compared to N_2-saturated electrolytes, confirming their effective CO_2 reduction capabilities. Notably, Ag_{20}-**Fc** delivered consistently higher current densities across the entire potential window, indicating superior CO_2RR kinetics and overall catalytic performance.

Gas chromatography (GC) analysis revealed that CO and H_2 were the only gaseous products formed during electrochemical CO_2 reduction, with no detectable liquid-phase products observed via ^1H NMR spectroscopy. This indicates a highly selective two-electron reduction pathway. All three Ag_{20}-based NCs demonstrated excellent selectivity toward CO, consistently achieving faradaic efficiencies (FE_{CO}) above 84% over a wide potential range (−0.6 to −1.8 V vs. RHE), underscoring the intrinsic activity of the Ag_{20} core for CO_2 electroreduction (Fig. 5B–D). However, the nature of the surface ligands had a pronounced impact on catalytic performance. Ag_{20}-**Fc**, functionalized with ferrocenylacetylene, exhibited the highest selectivity, maintaining FE_{CO} values above 98% from −1.0 to

−1.8 V, with a peak efficiency of 98.68% (Fig. 5E). In contrast, Ag_{20}-**Ph** and Ag_{20}-**OPh** (structure 2, containing CH_3CN molecules), modified with phenyl- and methoxyphenyl-acetylene ligands, showed lower maximum efficiencies, both remaining below 91%. Further insights were obtained by examining the CO partial current density (J_{CO}). At −1.8 V, Ag_{20}-**Fc** delivered a high J_{CO} of 157.54 mA cm^{-2}, far outperforming Ag_{20}-**Ph** (91.13 mA cm^{-2}) and Ag_{20}-**OPh** (73.50 mA cm^{-2}) (Fig. 5F). This enhancement highlights the role of the ferrocene moiety in promoting interfacial charge transfer, thereby improving catalytic efficiency. The turnover frequency (TOF) results corroborate these findings—Ag_{20}-**Fc** consistently exhibited higher TOF values across all applied potentials, confirming its superior intrinsic activity (Fig. 5G). To understand the origin of this enhanced performance, electrochemical impedance spectroscopy (EIS) was performed. Nyquist plots showed that Ag_{20}-**Fc** possesses lower charge transfer resistance than its counterparts, reflecting more efficient electron transport (Fig. S40). In addition, measurements of the electrochemically active surface area (ECSA) revealed a higher density of accessible active sites for Ag_{20}-**Fc** (Fig. S37–S39). These results collectively demonstrate that the unique electronic environment created by ferrocene ligands enhances both charge transport and active-site availability, leading to markedly improved CO_2 reduction
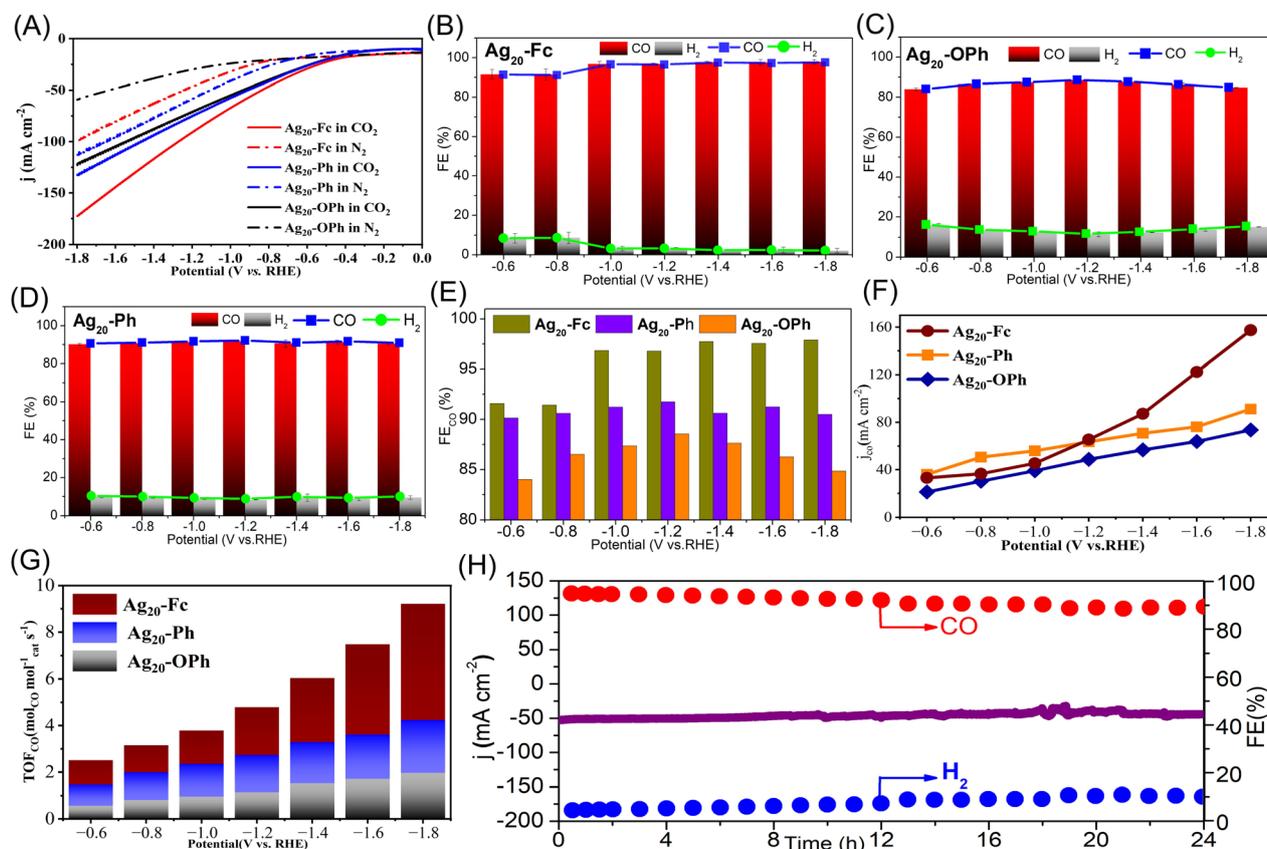

Fig. 5 (A) LSV of samples in N_2 or CO_2 saturated 1 M KOH solution; (B) FE values of Ag_{20}-**Fc** at different voltages; (C) FE values of Ag_{20}-**OPh** at different voltages; (D) FE values of Ag_{20}-**Ph** at different voltages; (E) comparison chart of FE_{CO} for three Ag_{20} clusters; (F) comparison chart of CO partial current density (j_{CO}) for three Ag_{20} clusters; (G) comparison chart of TOF values for three Ag_{20} clusters; (H) I–t test and FE_{CO} values of Ag_{20}-**Fc** at −1.0 V vs. RHE in different time periods.

performance. To assess the catalyst's durability, we conducted a rigorous 24-hour chronoamperometric test at -1.0 V. Throughout the test, the current density remained above 50 mA cm^{-2}, and the FE$_{CO}$ remained stable at over 90% (Fig. 5H). Additional characterizations, including powder X-ray diffraction (Fig. S41), ESI-MS (Fig. S42), X-ray photoelectron spectroscopy (Fig. S45), and transmission electron microscopy (Fig. S46), further confirmed that the catalyst retained its chemical composition and structural integrity throughout the electrolysis process.

To gain deeper insight into the origin of the enhanced catalytic activity imparted by ferrocene ligands, we carried out *in situ* electrochemical attenuated total reflection surface-enhanced infrared absorption spectroscopy (ATR-SEIRAS) measurements on **Ag$_{20}$-Fc** (Fig. 6A) and **Ag$_{20}$-Ph** (Fig. 6B) to monitor the evolution of key intermediates during the eCO$_2$RR process. Spectral changes were collected over a potential window from -0.6 to -1.8 V *vs.* RHE. A vibrational band at 1654 cm^{-1}, assigned to the O–H stretching mode of H$_2$O, indicates water activation and proton supply for PCET. Both catalysts display a characteristic absorption band at ~1380 cm^{-1}, attributable to the *COOH intermediate and corresponding to the C–OH stretching vibration.[56–58] The progressive increase in intensity of this band at more negative potentials reflects the accumulation of *COOH species as the reaction proceeds. Remarkably, **Ag$_{20}$-Fc** exhibits stronger and sharper *COOH signals than **Ag$_{20}$-Ph** under identical conditions, demonstrating more effective stabilization of intermediates and a more reactive catalytic interface. In addition, both catalysts exhibit a distinct absorption band near 2100 cm^{-1}, assigned to adsorbed *CO, accompanied by a simultaneous decrease of the CO$_2$ band at 2355 cm^{-1}, confirming continuous CO$_2$ consumption. Importantly, the *CO band of **Ag$_{20}$-Fc** is red-shifted by ~20 cm^{-1} relative to that of **Ag$_{20}$-Ph**, indicating weaker *CO binding on the **Ag$_{20}$-Fc** surface. Such weakened binding facilitates *CO desorption, thereby promoting CO release and enhancing turnover frequency. Collectively, these ATR-SEIRAS results demonstrate that **Ag$_{20}$-Fc** features faster electron-transfer kinetics and more favorable intermediate

dynamics, consistent with its superior CO$_2$ reduction performance.

To further elucidate the role of the ferrocenyl group in regulating the reactivity of Ag$_{20}$ NCs, we performed DFT calculations using **Ag$_{20}$-Fc** and **Ag$_{20}$-Ph** as model systems. The models were optimized based on their crystal structures, with the *tert*-butyl groups on TC4A replaced by H atoms to accelerate convergence. The optimized structures and corresponding Gibbs free energy diagrams for eCO$_2$RR and HER are shown in Fig. 7A. The calculations reveal that the formation of the *COOH intermediate is the rate-determining step of CO$_2$RR. The Gibbs free energy barrier for *COOH formation on **Ag$_{20}$-Fc** is 1.60 eV, lower than the 1.88 eV calculated for **Ag$_{20}$-Ph**, highlighting the energy advantage of Ag sites in **Ag$_{20}$-Fc** for CO$_2$-to-CO conversion (Fig. 7B). Since the two clusters share an identical metal framework and differ only in their alkynyl ligands, this discrepancy can be attributed to the electronic effect of the ferrocenyl group. The ferrocene moiety donates electrons to the Ag sites, rendering them more favorable for COOH formation. Moreover, the hydrogen adsorption free energy on **Ag$_{20}$-Fc** is 1.75 eV, higher than the 1.51 eV of **Ag$_{20}$-Ph**, suggesting that **Ag$_{20}$-Fc** is less favorable for H$_2$ evolution. Together, these findings demonstrate that ferrocenyl ligands not only stabilize critical *COOH intermediates but also suppress the competing HER, thereby enhancing the overall selectivity and activity of **Ag$_{20}$-Fc** toward CO$_2$ reduction.
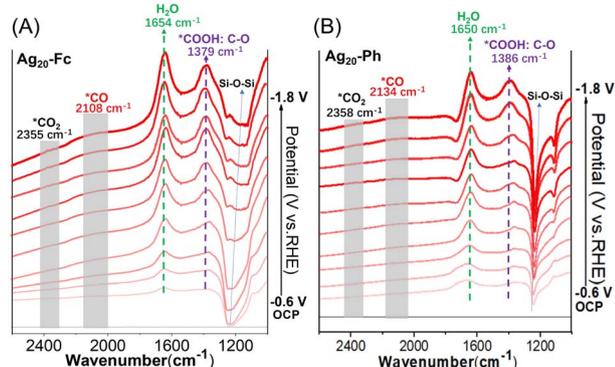

Fig. 6 ATR-FTIR test results of **Ag$_{20}$-Fc** (A) and **Ag$_{20}$-Ph** (B) in the 2600–1000 cm^{-1} range.
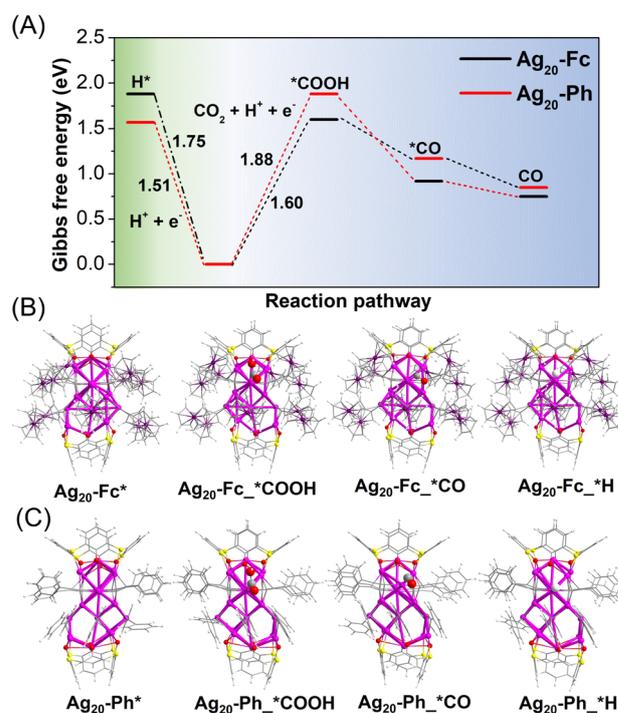
Fig. 7 (A) Free energy diagrams for the eCO$_2$RR and HER on **Ag$_{20}$-Fc** and **Ag$_{20}$-Ph**; (B) schematic diagram of the eCO$_2$RR process on **Ag$_{20}$-Fc**; (C) schematic diagram of the eCO$_2$RR process on **Ag$_{20}$-Ph**.

Conclusions

In conclusion, this work provides atomic-level insights into the structure–activity relationships of silver nanocluster catalysts for CO_2 reduction. We demonstrate that organometallic ligand engineering—particularly the incorporation of ferrocenylacetylene ligands—offers an effective strategy for precisely tuning the catalytic properties of atomically defined nanoclusters. Anchoring twelve ferrocenylacetylene ligands onto the well-defined **Ag$_{20}$-Fc** cluster yields markedly enhanced performance, achieving a CO faradaic efficiency above 98% with stable operation exceeding 24 h. *In situ* infrared spectroscopy and DFT calculations reveal that the ferrocenyl groups lower the energy barrier for key intermediates, highlighting the critical role of ligand–metal interactions in optimizing active-site environments. These findings not only deepen the understanding of ligand effects in CO_2 electroreduction but also establish a general design principle for developing highly efficient, tunable, and scalable nanocluster-based catalysts.

Author contributions

C. L. supervised the project and conceived the idea. H. Y. Z carried out synthesis, characterization and catalytic experiment of clusters. L. Y. L undertook the calculations for this article. H. Y. Z and C. L. wrote the manuscript. All authors discussed the experimental results.

Conflicts of interest

There are no conflicts of interest to declare.

Data availability

CCDC 2464030–2464033, 2464035, 2464036 and 2475347 contain the supplementary crystallographic data for this paper.[59a–g]

The data that support the findings of this study are available in the main text and the SI. Supplementary information: X-ray crystallographic file in CIF format, full experimental and computational details. See DOI: https://doi.org/10.1039/d5sc06306j.

Acknowledgements

Notes and references

1 L. L. Zhuo, P. Chen, K. Zheng, X. W. Zhang, J. X. Wu, D. Y. Lin, S. Y. Liu, Z. S. Wang, J. Y. Liu, D. D. Zhou and J. P. Zhang, *Angew. Chem., Int. Ed.*, 2022, **61**, e202204967.

2 Y. Song, W. Chen, C. Zhao, S. Li, W. Wei and Y. Sun, *Angew. Chem., Int. Ed.*, 2017, **56**, 10840–10844.

3 L. Li, X. Li, Y. Sun and Y. Xie, *Chem. Soc. Rev.*, 2022, **51**, 1234–1252.

4 J. Li, Y. Kuang, Y. Meng, X. Tian, W.-H. Hung, X. Zhang, A. Li, M. Xu, W. Zhou, C.-S. Ku, C.-Y. Chiang, G. Zhu, J. Guo, X. Sun and H. Dai, *J. Am. Chem. Soc.*, 2020, **142**, 7276–7282.

5 P. Deng, H. Wang, R. Qi, J. Zhu, S. Chen, F. Yang, L. Zhou, K. Qi, H. Liu and B. Y. Xia, *ACS Catal.*, 2019, **10**, 743–750.

6 H. Q. Fu, J. Liu, N. M. Bedford, Y. Wang, J. W. Sun, Y. Zou, M. Dong, J. Wright, H. Diao, P. Liu, H. G. Yang and H. Zhao, *Adv. Mater.*, 2022, **34**, 2202854.

7 Z. Tao, C. L. Rooney, Y. Liang and H. Wang, *J. Am. Chem. Soc.*, 2021, **143**, 19630–19642.

8 H. Seong, M. Choi, S. Park, H.-w. Kim, J. Kim, W. Kim, J. S. Yoo and D. Lee, *ACS Energy Lett.*, 2022, **7**, 4177–4184.

9 G. Wang, J. Chen, Y. Ding, P. Cai, L. Yi, Y. Li, C. Tu, Y. Hou, Z. Wen and L. Dai, *Chem. Soc. Rev.*, 2021, **50**, 4993–5061.

10 Q. Fan, P. Yan, F. Liu, Z. Xu, P. Liang, X. Cao, C. Ye, M. Liu, L. Zhao, S. Ren, H. Miao, X. Zhang, Z. Yang, X. Ding, J. Yang, C. Kong and Y. Wu, *Sci. Bull.*, 2024, **69**, 2881–2891.

11 Y. Yang, J. Fu, Y. Ouyang, T. Tang, Y. Zhang, L.-R. Zheng, Q.-H. Zhang, X.-Z. Liu, J. Wang and J.-S. Hu, *Natl. Sci. Rev.*, 2023, **10**, nwac248.

12 M. Zhang, M. Lu, M.-Y. Yang, J.-P. Liao, Y.-F. Liu, H.-J. Yan, J.-N. Chang, T.-Y. Yu, S.-L. Li and L. Y. Qian, *eScience*, 2023, **3**, 100116.

13 Y. Y. Birdja, E. Pérez-Gallent, M. C. Figueiredo, A. J. Göttle, F. Calle-Vallejo and M. T. M. Koper, *Nat. Energy*, 2019, **4**, 732–745.

14 X. Wang, M. H. Yu and X. L. Feng, *eScience*, 2023, **3**, 100141.

15 D. Wang, J. J. Mao, C. C. Zhang, J. W. Zhang, J. S. Li, Y. Zhang and Y. F. Zhu, *eScience*, 2023, **3**, 100119.

16 P. Li, J. Bi, J. Liu, Q. Zhu, C. Chen, X. Sun, J. Zhang and B. Han, *Nat. Commun.*, 2022, **13**, 1965.

17 H. Li, T. Liu, P. Wei, L. Lin, D. Gao, G. Wang and X. Bao, *Angew. Chem., Int. Ed.*, 2021, **60**, 14329–14333.

18 R.-X. Meng, C.-L. Zhao, P.-L. Luo, Y.-Q. Tian, Q. Tang, L.-K. Wang, J. Yan and C. Liu, *Chem. Sci.*, 2025, **16**, 6845–6852.

19 S. Zhuang, D. Chen, W. Fan, J. Yuan, L. Liao, Y. Zhao, J. Li, H. Deng, J. Yang, J. Yang and Z. Wu, *Nano Lett.*, 2022, **22**, 7144–7150.

20 C. Du, J. P. Mills, A. G. Yohannes, W. Wei, L. Wang, S. Lu, J.-X. Lian, M. Wang, T. Guo, X. Wang, H. Zhou, C.-J. Sun, J. Z. Wen, B. Kendall, M. Couillard, H. Guo, Z. Tan, S. Siahrostami and Y. A. Wu, *Nat. Commun.*, 2023, **14**, 6142.

21 Y. Gao, Q. Wu, X. Liang, Z. Wang, Z. Zheng, P. Wang, Y. Liu, Y. Dai, M. H. Whangbo and B. Huang, *Adv. Sci.*, 2020, **7**, 1902820.

22 H. Seong, K. Chang, F. Sun, S. Lee, S. M. Han, Y. Kim, C. H. Choi, Q. Tang and D. Lee, *Adv. Sci.*, 2023, **11**, 2306089.

23 L. J. Liu, Z. Y. Wang, Z. Y. Wang, R. Wang, S. Q. Zang and T. C. W. Mak, *Angew. Chem., Int. Ed.*, 2022, **61**, e202205626.

24 G. Deng, H. Yun, M. S. Bootharaju, F. Sun, K. Lee, X. Liu, S. Yoo, Q. Tang, Y. J. Hwang and T. Hyeon, *J. Am. Chem. Soc.*, 2023, **145**, 27407–27414.

25 Z.-H. Gao, K. Wei, T. Wu, J. Dong, D.-e. Jiang, S. Sun and L.-S. Wang, *J. Am. Chem. Soc.*, 2022, **144**, 5258–5262.

26 Y. Q. Tian, W. L. Mu, L. L. Wu, X. Y. Yi, J. Yan and C. Liu, *Chem. Sci.*, 2023, **14**, 10212–10218.

27 L. J. Li, W. L. Mu, Y. Q. Tian, W. D. Yu, L. Y. Li, J. Yan and C. Liu, *Chem. Sci.*, 2024, **15**, 7643–7650.

28 Z. Wang, L. Li, L. Feng, Z. Y. Gao, C. H. Tung, L. S. Zheng and D. Sun, *Angew. Chem., Int. Ed.*, 2022, **61**, e202200823.

29 K. Sheng, B. L. Han, Z. Wang, Z. Y. Gao, C. H. Tung and D. Sun, *Angew. Chem., Int. Ed.*, 2024, **64**, e202416065.

30 S. Biswas, A. K. Das, S. S. Manna, B. Pathak and S. Mandal, *Chem. Sci.*, 2022, **13**, 11394–11404.

31 L.-J. Li, Y.-T. Luo, Y.-Q. Tian, P. Wang, X.-Y. Yi, J. Yan, Y. Pei and C. Liu, *Inorg. Chem.*, 2023, **62**, 14377–14384.

32 W.-D. Si, H. Liang, S.-H. Ji, T. Kim, C. K. Zhang, Z. Wang, H.-F. Su, C.-H. Tung and D. Sun, *J. Am. Chem. Soc.*, 2025, **147**(36), 32458–32467.

33 H. Zhao, C. Zhang, B. Han, Z. Wang, Y. Liu, Q. Xue, C.-H. Tung and D. Sun, *Nat. Synth.*, 2024, **3**, 517–526.

34 Y. Chen, X. Zhou, X. Liu, Z. Tang, L. Wang and Q. Tang, *J. Am. Chem. Soc.*, 2025, **147**, 2699–2713.

35 X. Ma, F. Sun, L. Qin, Y. Liu, X. Kang, L. Wang, D.-e. Jiang, Q. Tang and Z. Tang, *Chem. Sci.*, 2022, **13**, 10149–10158.

36 G. Deng, J. Kim, M. S. Bootharaju, F. Sun, K. Lee, Q. Tang, Y. J. Hwang and T. Hyeon, *J. Am. Chem. Soc.*, 2022, **145**, 3401–3407.

37 S. Yoo, D. Kim, G. Deng, Y. Chen, K. Lee, S. Yoo, X. Liu, Q. Tang, Y. J. Hwang, T. Hyeon and M. S. Bootharaju, *J. Am. Chem. Soc.*, 2025, **147**, 12546–12554.

38 S.-F. Yuan, Z.-J. Guan and Q.-M. Wang, *J. Am. Chem. Soc.*, 2022, **144**, 11405–11412.

39 W.-L. Mu, L.-Y. Li, X.-Z. Cong, P.-K. Xia, X.-Y. Chen, Q.-Y. Liu, L.-K. Wang, J. Yan and C. Liu, *J. Am. Chem. Soc.*, 2024, **146**, 28131–28140.

40 X.-Y. Chen, L.-Y. Li, L.-C. Zhao, Q.-Y. Liu, D.-D. Ding, L.-K. Wang, H.-B. Mo, J. Yan and C. Liu, *Angew. Chem., Int. Ed.*, 2025, e202511232.

41 J. L. Hou, N. H. Huang, D. Acharya, Y. X. Liu, J. Y. Zhu, J. X. Teng, Z. Wang, K. Q. Qu, X. X. Zhang and D. Sun, *Chem. Sci.*, 2024, **15**, 2655–2664.

42 J. Y. Xu, L. Xiong, X. Cai, S. S. Tang, A. C. Tang, X. Liu, Y. Pei and Y. Zhu, *Chem. Sci.*, 2022, **13**, 2778–2782.

43 H.-N. Zhou, L.-Y. Li, Y.-X. Li, H.-B. Mo, J. Yan and C. Liu, *Chin. Chem. Let*, 2025, **15**, 111269.

44 J.-H. Huang, H. Zhang, Z.-Y. Wang, J.-H. Hu, J. Li, J. Cai and S.-Q. Zang, *J. Am. Chem. Soc.*, 2025, **147**, 16593–16601.

45 V. K. Kulkarni, B. N. Khiarak, S. Takano, S. Malola, E. L. Albright, T. I. Levchenko, M. D. Aloisio, C.-T. Dinh, T. Tsukuda, H. Häkkinen and C. M. Crudden, *J. Am. Chem. Soc.*, 2022, **144**, 9000–9006.

46 T. Jia, Y.-X. Li, X.-H. Ma, M.-M. Zhang, X.-Y. Dong, J. Ai and S.-Q. Zang, *Nat. Commun.*, 2023, **14**, 6877.

47 Q. Yuan, S. Huang, H. Lin, G. Saranya, W. Hu, G. Li, X. Cai, X. Liu, M. Chen, W. Ding and Y. Zhu, *ACS Catal.*, 2023, **13**, 16188–16194.

48 J. Wang, X. Huang, S. Xi, H. Xu and X. Wang, *Angew. Chem., Int. Ed.*, 2020, **59**, 19162–19167.

49 M. G. Walawalkar, P. Pandey and R. Murugavel, *Angew. Chem., Int. Ed.*, 2021, **60**, 12632–12635.

50 G. Deng, H. Yun, Y. Chen, S. Yoo, K. Lee, J. Jang, X. Liu, C. W. Lee, Q. Tang, M. S. Bootharaju, Y. J. Hwang and T. Hyeon, *Angew. Chem., Int. Ed.*, 2024, **64**, e202418264.

51 Z. Xin, Y.-R. Wang, Y. Chen, W.-L. Li, L.-Z. Dong and Y.-Q. Lan, *Nano Energy*, 2020, **67**, 104233.

52 H. Zhang, S. Si, G. Zhai, Y. Li, Y. Liu, H. Cheng, Z. Wang, P. Wang, Z. Zheng, Y. Dai, T. X. Liu and B. Huang, *Appl. Catal., B*, 2023, **337**, 122909.

53 J. Liang, X. Gao, B. Guo, Y. Ding, J. Yan, Z. Guo, E. C. M. Tse and J. Liu, *Angew. Chem., Int. Ed.*, 2021, **60**, 12770–12774.

54 S. Yoo, S. Yoo, G. Deng, F. Sun, K. Lee, H. Jang, C. W. Lee, X. Liu, J. Jang, Q. Tang, Y. J. Hwang, T. Hyeon and M. S. Bootharaju, *Adv. Mater.*, 2023, **36**, 2313023.

55 J. Yan, B. K. Teo and N. Zheng, *Acc. Chem. Res.*, 2018, **51**, 3084–3093.

56 Z. J. Guan, R. L. He, S. F. Yuan, J. J. Li, F. Hu, C. Y. Liu and Q. M. Wang, *Angew. Chem., Int. Ed.*, 2022, **61**, e202116965.

57 J. Wang, F. Xu, Z. Y. Wang, S. Q. Zang and T. C. W. Mak, *Angew. Chem., Int. Ed.*, 2022, **61**, e202207492.

58 X.-K. Wan, J.-Q. Wang, Z.-A. Nan and Q.-M. Wang, *Sci. Adv.*, 2017, **3**, e1701823.

59 (*a*) CCDC 2464030: Experimental Crystal Structure Determination, 2025, DOI: **10.5517/ccdc.csd.cc2nq0v8**; (*b*) CCDC 2464031: Experimental Crystal Structure Determination, 2025, DOI: **10.5517/ccdc.csd.cc2nq0w9**; (*c*) CCDC 2464032: Experimental Crystal Structure Determination, 2025, DOI: **10.5517/ccdc.csd.cc2nq0xb**; (*d*) CCDC 2464033: Experimental Crystal Structure Determination, 2025, DOI: **10.5517/ccdc.csd.cc2nq0yc**; (*e*) CCDC 2464035: Experimental Crystal Structure Determination, 2025, DOI: **10.5517/ccdc.csd.cc2nq10g**; (*f*) CCDC 2464036: Experimental Crystal Structure Determination, 2025, DOI: **10.5517/ccdc.csd.cc2nq11h**; (*g*) CCDC 2475347: Experimental Crystal Structure Determination, 2025, DOI: **10.5517/ccdc.csd.cc2p2sxh**.